Journal of Scientific & Industrial Research
Vol. 85, April 2026, pp. 364-377
DOI: 10.56042/jsir.v85i4.4173

Investigation of Micro Electrical Discharge Drilling on Fabricated Zn/(Fe+Ag+Mg)-MMC for Cardiovascular Stent Application

Pankaj Mohan[1], Prashant Chechi[2], Saurabh Kumar Maurya[1]* & Alakesh Manna[1]
[1]Department of Mechanical Engineering, Punjab Engineering College (Deemed to be University), Chandigarh 160 012, India
[2] University Centre for Research and Development, Chandigarh University, Mohali 140 413, Punjab, India

Received 19 July 2023; revised 24 October 2025; accepted 14 May 2026

These days, zinc and its composites have attracted significant interest in the field of biomedical engineering due to their bio absorbability. Micro Electrical Discharge Drilling (μ-EDD) was used for making micro perforations in Zn/(Fe+Ag+Mg)-MMC for cardiovascular stent application. The influence of μ-EDD process parameters such as peak current, pulse-off time, pulse-on time, tool rotation, tool material, and electrode polarity were studied with respect To Material Removal Rate (MRR), Drill Overcut (DO), and Tool Wear Rate (TWR) during the micro-drilling of the MMC. Further, Taguchi and GRA based optimization were performed. From the experimental study it was found that MRR, DO and TWR increases with peak current, pulse-on-time and rotation of tool electrode. Optimization improved the MRR, DO and TWR by 111.52%, 20.83% and 76.79% respectively. Peak current and pulse-on-time was found significant for MRR DO and TWR whereas peak current and pulse-off-time was found significant for GRA based analysis. SEM examinations of the micro-drilled hole show that high circularity and a good surface finish was achieved.

Keywords: Biodegradable stents, Hybrid metal matrix composite, Micro perforation, SEM analysis, Ultrasonic vibration-aided stir casting

Introduction

Over the last decade, polymeric material such as Poly-L-Lactic acid and metallic materials such as stainless steel, magnesium, cobalt, nitinol etc. have been extensively studied as potential bio-degradable stent materials.[1,2] Concerns over the use of polymers have been reported due to their poor mechanical strength, rapid and slow degradation rates of magnesium and iron respectively.[3] Despite biocompatibility and biodegradability of polymeric stents like PLLA (Poly-L-lactic acid), its intrinsic low mechanical properties notably constrain its clinical performance in vascular stents.[4,5] Magnesium based biodegradable stents were once considered promising because of their good biocompatibility, but they tend to degrade faster than expected. This rapid degradation releases hydrogen gas and increases the surrounding pH, which ultimately causes the stent to lose its structural strength earlier than needed.[5,6] In contrast, iron-based biodegradable stents break down at a very slow rate, leading to the buildup of bulky, rust-like corrosion deposits. Their ferromagnetic nature also poses safety concerns during MRI scans, which limits their suitability for clinical use.[7,8] Nitinol based bare metal stents, while offering excellent flexibility and super elasticity, have disadvantages including their permanence in the vessel, which can lead to chronic inflammation, late stent thrombosis, and complications in re-interventions, as well as potential nickel hypersensitivity reactions in some patients.[9] At the same time Cobalt–chromium stents provide high radial strength and thin struts, yet they remain susceptible to restenosis and late thrombosis, and the release of nickel or cobalt ions may trigger hypersensitivity reactions and inflammatory responses in sensitive individuals.[10]

From the in-vivo degradation study of pure zinc wires in the abdominal aorta of a Sprague-Dawley rat, it was found that zinc exhibits ideal corrosion behaviour for bio absorbable stents. As the implant underwent partial degradation, tissue regeneration occurred within its initial implantation site. The sparse cellular distribution and lack of smooth muscle cells near the implant interface suggests that zinc may inhibit cell proliferation and help prevent restenosis after stent implantation.[11,12] Hiebl *et al*. evaluated the biocompatibility and degradation behaviour of a zinc-based stent and reported that the closed-design zinc

*Author for Correspondence
E-mail: skks.saurabh@gmail.com

stent was non-cytotoxic. They also observed that its degradation characteristics were more favourable when compared with magnesium and stainless steel stents.[13] Yang *et al*. implanted pure zinc stents in the abdominal aorta of three rabbits for a period of 12 months. The results showed that the stents retained sufficient mechanical strength for about 6 months and exhibited a volume loss of nearly 41.75 ± 29.72% after one year of implantation. No serious issues such as inflammation, platelet adhesion, thrombosis, or notable intimal thickening were detected. Moreover, the gradual degradation of the zinc stent was found to support arterial remodelling and the natural healing process.[14] Liu *et al*. examined the corrosion behaviour of pure zinc in revised simulated body fluid (r-SBF) for up to 336 hours. During the early stages, the corrosion layer was mainly formed of oxidation products of zinc along with zinc–calcium phosphate compounds. The results showed that corrosion behaviour of pure zinc was predominantly uniform with a corrosion rate in the range of 0.02 to 0.07 mm per year, indicating its good potential for biomedical use.[15] Li *et al*. studied the mechanical characteristics, cytotoxicity, antibacterial properties and in-Vitro degradation of Zn-4.0Ag alloy. The corrosion rate of Zn-4Ag alloy was greater than that of pure zinc. The results show that Zn-4.0Ag can be a promising candidate for biodegradable implants.[16] Kafri *et al.* studied the suitability of Zn-1.3%Fe alloy as a biodegradable implant material. Adding iron (Fe) to zinc increases its corrosion rate under both in-vitro and in-vivo conditions. During 14 weeks of implantation, no harmful systemic effects were observed in the rats, as reflected by normal body weight gain, regular activity, and stable hematological parameters such as RBC, HGB, and WBC.[17] Niu *et al.* studied the mechanical properties, antibacterial evaluation, in-vitro degradation and cytotoxicity of the as-extruded Zn-4Cu alloy and found it as suitable for cardiovascular stent application.[18] Mostaed *et al.* found that addition of Mg refines the grain size of Zn-Mg alloy. Also, extruded alloys showed higher corrosion resistance as compared to the as-cast alloys. Among the alloys that were studied, Zn–0.5 wt% Mg showed the most balanced improvement in strength and ductility, making it one of the most promising candidates for stent applications.[19] Vojtech *et al.* examined corrosion properties of Zn-Mg alloys for the potential applications in bone fixation. They found Zn-Mg alloy has higher strength and corrosion resistance than pure Zn and pure Mg in simulated body fluids.[20] Sikora-Jasinska *et al*. developed Zn-Ag alloys fabricated using casting process followed by hot extrusion. The findings revealed hot extrusion significantly decreases the grain size of alloy and increases the mechanical properties compared to pure zinc. Also, the degradation rate of Zn-Ag alloy was slightly faster than pure zinc.[21] Zhao *et al*. developed a Zn-based Zn-Li alloy and based on its mechanical and degradation behaviour they claimed it as another promising bio-degradable vascular stent material.[22] Hehrlein *et al*. casted and extruded zinc-based alloys and found them mechanically stable for the bio absorbable vascular stents application. The degradation rate of Zn-1Mg alloy was 0.12–0.28 mm/y whereas, Zn-3Ag alloy was 0.16 mm/y.[23] A comparison between zinc, magnesium and stainless steel for cardiovascular stents shows that stainless steel has very little degradation while magnesium has very large degradation rate. The degradation rate of zinc lies between the both.[24] Radioactive stents carries radiation-related risks and complex regulatory challanges.[25] Biodegradable polymeric stents suffer from low tensile strength, limited ability to withstand pulsatile vascular loads, and require thick struts that may disturb blood flow.[4,5] On the other hand, Drug-eluting permanent metal stents provide strong mechanical support but are associated with chronic inflammation, late thrombosis, and polymer-related hypersensitivity.[26] These limitations collectively represent the major causes of stent failure, including insufficient mechanical strength, uncontrolled degradation, and inflammation-induced late thrombosis.

These days, the demand of the miniature products is increasing day by day. In the industries like biomedical, aerospace, micro-cooling equipment, UV photodiodes, micro-lens, electronics etc.[27] micro-components are fabricated by utilising micro-machining. Unconventional machining methods are found most appropriate for micro-machining of hard and difficult to machine materials. Conventional methods can also be used for producing the micro holes, but rapid tool breakage and dimensional inaccuracy are the biggest challenge associated with the conventional micro-machining. them. Therefore, the demand of the non-traditional micro-machining processes like; Electrical Discharge Drilling (EDD), Laser Beam Machining (LBM), Abrasive Water Jet Machining (AWJM) has been significantly increased.[28] Micro-Electrical Discharge Drilling (μ-EDD) can be efficiently used to produce very small and complicated shapes.[29] In μ-EDD, discrete sparks are produced between the tool electrode and workpiece specimen. The high heat produced due to the generation of these sparks that causes the melting and evaporation of work material. The flushing of the removed material from the surface is accomplished by high pressure dielectric supply through the rotating tabular electrode. [30] In μ-EDD, the tool electrode has no direct physical contact with the workpiece material. which eliminated the challenges associated with the conventional machining.[31] In the micro-machining the machining responses such as material removal rate, radial overcut, drill taper, surface finish, dimensional accuracy tool wear rate etc. are greatly influenced by the process parameters such as voltage, current, pulse-on-time, pulse off time, rotation of tool electrode, tool electrode material etc.[32] Therefore, it is crucial to know the right value of the process parameters to improve the surface quality and dimensional accuracy of the micro-drilled hole in very cost effective manner.

Based on the review of literature it was found that zinc and alloys can be effectively used for the cardiovascular stent application and μ-EDD can be efficiently utilised to create micro-perforation on the conductive materials. Previous studies have reported that the addition of Fe, Ag, and Mg to zinc-based systems can improve fatigue resistance, refine microstructure, and impart antibacterial functionality, while the Zn matrix has been associated with enhanced endothelial healing and reduced chronic inflammation.[33,11] These attributes highlights the potential of Zn-based hybrid composite for biodegradable stent applications. Therefore, in the current research work, a novel Zn/(Fe+Ag+Mg)-MMC was produced by utilising ultrasonic vibration-aided stir casting, rolled and heat treated to enhance the mechanical and bio-degradation properties. Apart from that, micro-perforation was accomplished on the fabricated Zn/(Fe+Ag+Mg)-MMCs utilising μ-EDD. Zn is a low-density material and drilling of Zn alloys and composites is faster as compared to the other metals and jamming of sparks occur during deep drilling. From the literature it was also found that, there is very less available data on micro-machining of Zn-MMCs. Therefore, a detailed experimental investigation had been performed during micro-perforation of newly developed Zn/(Fe+Ag+Mg)-MMC using One-Factor-at-a-Time (OFAT) approach to evaluate the effect of each process parameter on responses and obtaining the best range of the same. The effect of process variables such as peak current, pulse-on-time, pulse-off-time, rotation of tool electrode, tool material and electrode polarity on the responses has been identified while micro-machining of fabricated specimen. Further, optimization of the process parameters was performed based on Taguchi and Grey Relational Analysis (GRA) determine the optimal parametric combination of process parameters to maximize the MRR and minimize the DO & TWR. ANOVA was also performed to find out the significant parameters for responses. Scanning Electrode Microscopy (SEM) examination of machined surface was also performed to see the morphology generated during micro-machining of Zn-MMCs.

Materials and Methods

In the current experimental study, ultrasonic vibration-aided stir casting technique was utilised for the development of hybrid Zn/(Fe+Ag+Mg)-MMC.[34,35] The metal powder of Fe, Ag and Mg produced by rotary electrode atomization method was used as reinforcement. Retsch, MM400 powder ball mixing machine was used to mix the 1 wt% Fe powders, 1 wt% Ag and 0.5 wt% Mg powders. The average particle size of the Fe, Ag, Mg metal powder was 37 μm. The resistance heated furnace was employed to melt the zinc ingot at a temperature of 550°C and mixture of Fe-Ag-Mg powders was heated at 400°C in a separate furnace Mixing of melted Zn matrix with reinforcement were obtained by stirring it for 15 minutes at 300 rpm in presence of Argon gas. The study made use of a Hitsan ultrasonic vibration transducer operating at 40 kHz for producing ultrasonic vibrations in the molten mixture. The melt was subsequently heated again to 550°C and held for 15 minutes to regain optimal fluidity. After that, the molten material was cast into an E0300 alloy steel die cavity. A preheating treatment at 300°C for three hours was applied to the cast Zn/(Fe+Ag+Mg) hybrid composite samples in a resistance heating furnace under an argon atmosphere and then subjected to hot rolling. The hot rolling process was performed at a roll speed of 12 rpm, reducing the cast sample thickness from 10 mm to 2 mm, with each pass decreasing the thickness by 0.2 mm. After hot rolling, the hybrid Zn/(Fe+Ag+Mg) MMC samples were subjected to further heat treatment to enhance their mechanical properties. Solution heat treatment was carried out by holding the rolled samples at 380 °C for 15 hours in a resistance heating furnace, followed

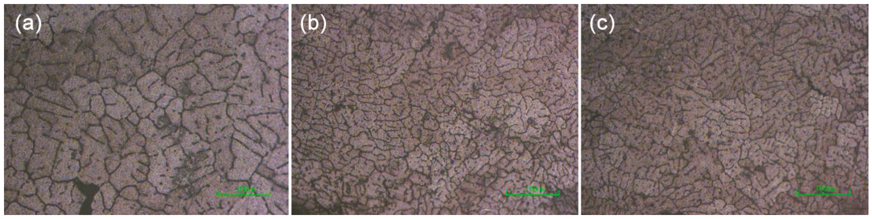

Fig. 1 — Micro structure of hybrid Zn/(Fe+Ag+Mg)-MMC: (a) stir casted, (b) stir casted + Hot rolled, (c) Stir casted+ hot rolled+ heat treated

Table 1 — Mechanical test resultsfor Zn/(Fe+Ag+Mg)-MMC

Zn/(Fe+Ag+Mg)-MMC	Density (g/cc)	Yield strength (MPa)	Ultimate tensile strength (MPa)	Elongation (%)	Micro-hardness (Vickers)
Stir Casted	7.68	158.42	179.35	14.26	39.61
Stir casted + hot rolled	7.95	309.76	392.36	54.29	47.29
Stir casted+ hot rolled+ heat treated	7.74	251.26	326.52	60.78	49.48

by rapid quenching in 10°C deionised water. The microstructural characteristics of the fabricated Zn/(Fe+Ag+Mg)-MMC under various processing conditions are presented in Fig. 1. The mechanical properties measured for the hybrid Zn/(Fe+Ag+Mg) MMCs produced through ultrasonic vibration–aided stir casting, followed by hot rolling and heat treatment are summarised in Table 1. Based on the mechanical properties, stir casted+ hot rolled+ heat treated Zn/(Fe+Ag+Mg)-MMC was found to be used suitable for cardiovascular stent application and used for further μ-electrical discharge drilling investigation.

Result and Discussion

Preliminary Experiments

A 3-axis micro electrical discharge machining setup was used to produce the micro drill on the Zn/(Fe+Ag+Mg) MMC. It is also known as the first drill EDM. For obtaining the impact of individual process parameters during μ-EDD of fabricated MMC, experiments were conducted using OFAT approach i.e. varying one process parameter and keeping other parameters at their mid-range. The process parameters and their corresponding ranges used for conducting the preliminary experiments are presented in Table 2. The μ-EDD machine, control panel, and micro-drilled workpiece specimen are shown in Fig. 2(a–c), respectively.

Performance Characteristic

The influence of μ-EDD process parameters on key performance responses specifically drill overcut (DO), material removal rate (MRR), and tool wear rate (TWR) was examined while micro-drilling of stir casted + hot rolled + heat-treated hybrid Zn/(Fe+Ag+Mg)-MMC specimens.

Table 2 — Working ranges of the selected process parameters

Sr. No.	Process parameter	Working range		Unit
		Minimum	Maximum	
1	Peak current	1	9	A
2	Pulse-on-time	10	90	μs
3	Pulse-off-time	10	90	μs
4	Tool rotation	100	160	rpm
5	Tool material	Copper	Brass	—

The values of MRR, DO, and TWR can be obtained using the following relations:

$$\text{MRR (mg/min)} = (W_i - W_f)/t \quad \dots (1)$$

$$\text{DO } (\mu\text{m}) = D_{avg} - D_{tool} \quad \dots (2)$$

$$\text{TWR (mm/min)} = \text{TWL}/t \quad \dots (3)$$

where, W_i = weight initial; W_f = weight final; TWL = tool wear length; t = time; D_{avg} = average diameter of drilled hole; D_{tool} = diameter of tool; t = time taken for drilling hole.

Effect of Process Parameters on Output Responses

The effects of different input process parameters on MRR, DO and TWR based on the OFAT approach are shown in Figs 3–5.

From the Fig. 3 (a, b), Fig. 4 (a, b) and Fig. 5 (a, b) it can be seen that as peak current and pulse-on-time increases, MRR, DO and TWR all are increases. As the peak current and pulse-on-time increases, high intensity spark generated for the longer period of time in the neighbourhood area of tool electrode and workpiece. The amount of spark energy produced at the interface between the tool and the workpiece depends on the applied voltage, peak current, and pulse-on time. This energy causes localized melting and evaporation of the workpiece material at the tool–workpiece contact zone.[36] Consequently, higher

MRR, RO and TWR are acquired. A rise in the peak current and pulse-on-time gradually increases the MRR, DO and TWR but a sharp increment was seen past 7 A peak current and 70 s pulse-on-time, beyond this limit of peak current and pulse-on-time, the machining was unstable and which results rapid tool wear and worsen drilled hole quality. Hence peak current and pulse-on-time values are not recommended beyond this limit.

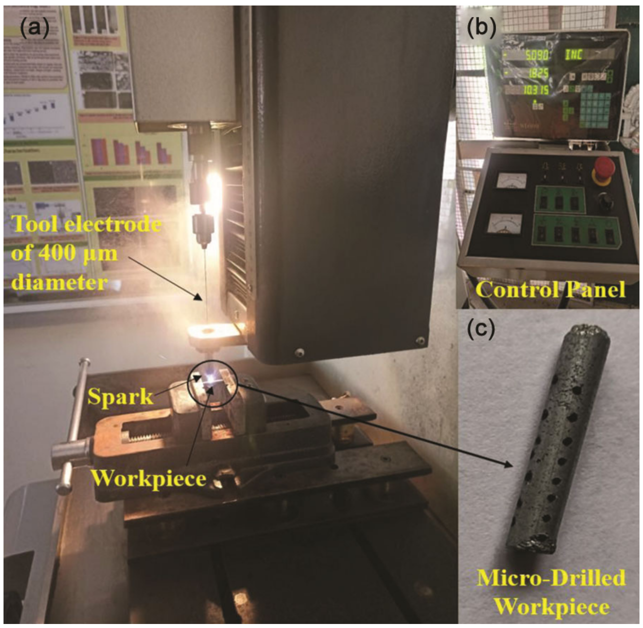

Fig. 2 —µ-EDD experimental setup and drilled specimen: (a) µ-EDD machining setup, (b) Control panel, and (c) Micro-drilled work piece specimen

From the Figs 3(c), 4(c) and 5(c), it is clear that as pulse-off-time increases, MRR, DO and TWR all decreases. It is because of higher dwell period (time between repetitive sparks) at higher pulse-off-time. Due to this, frequency of sparks generation decreases hence lower melting and evaporation of the material takes place at the tool-workpiece interface and results lower MRR, DO and TWR.[37] MRR and TWR increase up to 140 and 150 rpm, respectively, as illustrated in Figs 3(d) and 5(d). If the tool rotation further increases both MRR and TWR decreases. With the higher tool rotation, more clearance of the molten debris from the melted pool can be achieved. It every time exposed a fresh workpiece surface to the tool electrode and which leads the better spark intensity generation. Consequently, higher temperature reached at the tool-workpiece interface and more material removal takes place from tool and workpiece surfaces. As the tool rotation further increases i.e. beyond 140 rpm for MRR and 150 rpm for TWR, the MRR and TWR was found decreased, it

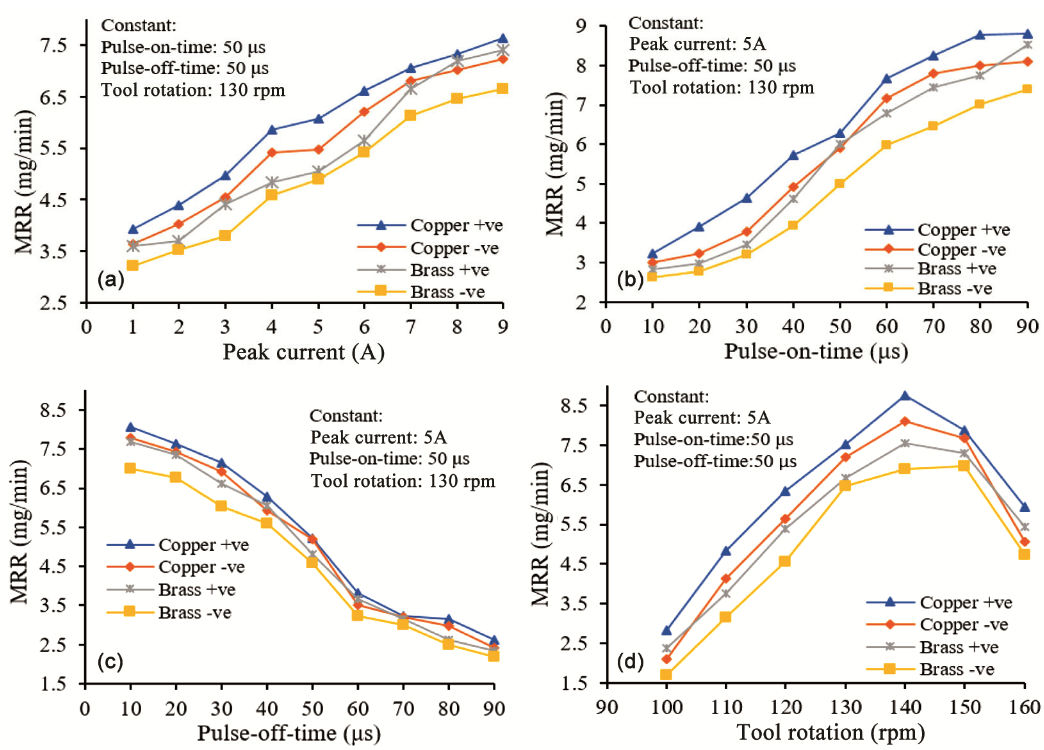

Fig. 3 — Effect of process parameters on Material Removal Rate (MRR): (a) Peak Current (A), (b) Pulse-on Time (µs), (c) Pulse-off Time (µs), and (d) Tool Rotation (rpm) for copper and brass tools under positive and negative polarity conditions

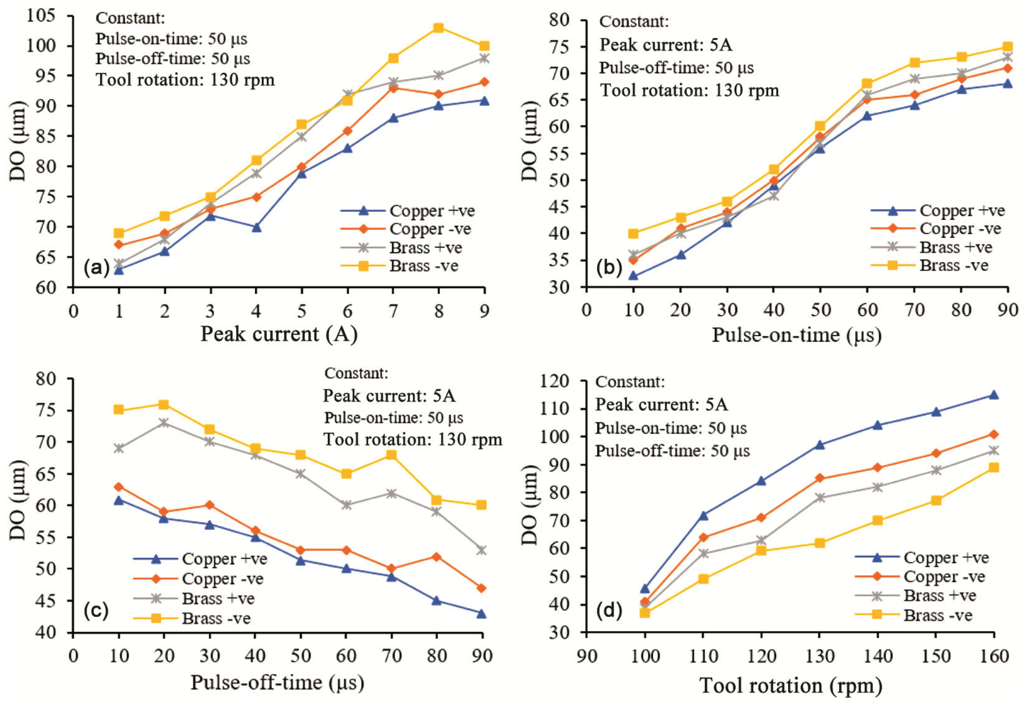

Fig. 4 — Effect of process parameters on Drill Overcut (DO): (a) Peak Current (A), (b) Pulse-on Time (µs), (c) Pulse-off Time (µs), and (d) Tool Rotation (rpm) for copper and brass tools under positive and negative polarity conditions

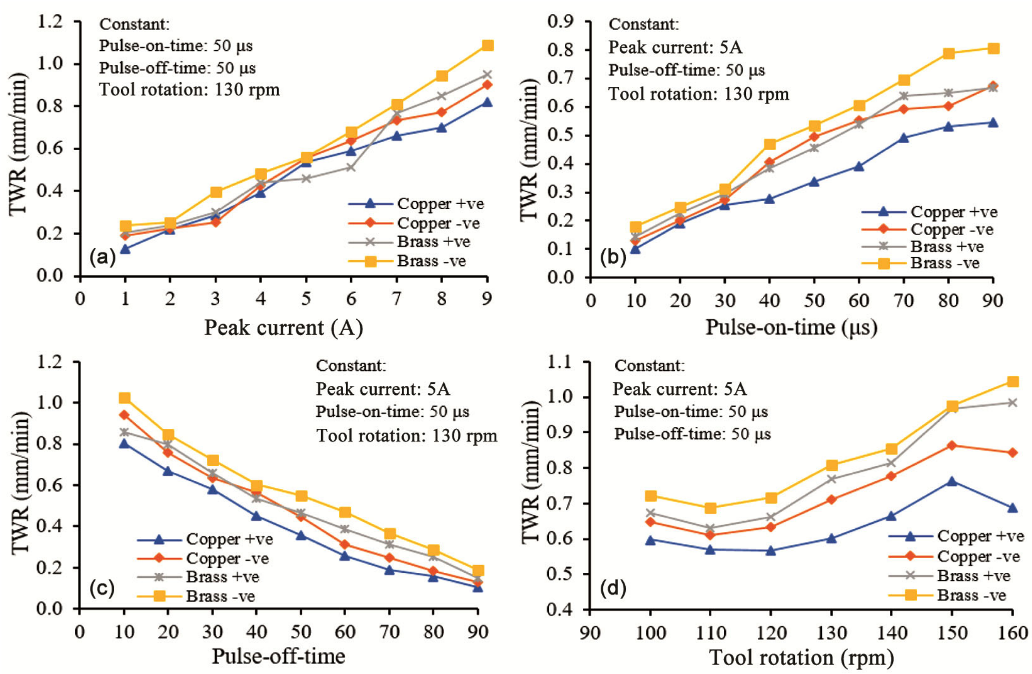

Fig. 5 — Effect of process parameters on Tool Wear Rate (TWR): (a) Peak Current (A), (b) Pulse-on Time (µs), (c) Pulse-off Time (µs), and (d) Tool Rotation (rpm) for copper and brass tools under positive and negative polarity conditions

may to be due to the centrifugal effect produced by tool rotation and which transferred to the molten debris and molten debris sticks back to the workpiece. Therefore, lower intense spark generated in the vicinity of tool & workpiece and lowers the MRR & TWR. Also, as the rotation of the tool increases; DO increases due to the vibration created by the rotary tool (Fig. 4 (d)). The thermos-physical properties of tool electrode material also influence the response characteristics.[38] Copper outperforms other tool materials because its high electrical conductivity produces stable and consistent sparks, improving energy transfer to the workpiece surface. Its excellent thermal conductivity rapidly dissipates heat, which helps preserve the tool shape and reduces thermal damage during repeated discharges resulting in lower tool wear.

From the Figs 3–5, it is clear that machining with copper tool electrode results better performance for MRR, DO and TWR. Further, polarity of tool electrode also plays a stimulating role on the response characteristics over the course of micro-drilling of developed Zn/(Fe+Ag+Mg)-MMCs. It was observed that machining with positive tool polarity offers better outcomes in terms of MRR, DO and TWR, when compared to the machining with negative tool polarity. In positive polarity, tool connected to negative terminal and workpiece connected to the positive terminal and results lesser erosion of tool. Although conventional EDD often shows higher tool wear under positive polarity, in µ-EDD the extremely low discharge energy and copper's superior thermal management significantly suppress thermal erosion, leading to comparatively lower tool wear and improved machining stability. These combined effects deliver enhanced machining efficiency, higher material removal, and smoother hole surfaces. The similar observations were also reported by Kumar *et al.*[29] Therefore, copper tool electrode under positive tool electrode polarity is suggested for the detailed experiments.

Table 3 — Process variables and their levels

Process parameters	Level 1	Level 2	Level 3	Level 4	Unit
Peak current (A)	3	4	5	6	A
Pulse-on-time (B)	40	50	60	70	µs
Pulse-off-time (C)	20	30	40	50	µs
Tool rotation (D)	110	120	130	140	rpm

Detailed Experiments and Optimization of Parameters

Based on the preliminary tests results, range of peak current pulse-on-time, pulse-off-time and tool rotation were selected for the detailed experiments and shown in Table 3. Copper tool electrode under positive polarity was used for performing entire set of detailed experiments. Taguchi's L_{16} Orthogonal Array (OA) was employed for the design of experiments. As per Table 3 and Taguchi's L_{16} orthogonal array, there were 48 experiments were performed (triplicate) and the averaged results of the measured output responses were selected for further investigation. The average responses along with S/N ratio value i.e. signal to noise ratio are presented in Table 4.

Optimization of Responses based on Taguchi

Using the different S/N ratio values listed in Table 4, the S/N ratio plots for MRR, DO, and TWR were generated and are presented in Fig. 6(a–c), respectively. From Fig. 6(a), it can be seen that the optimal set of parameters for MRR is A4B4C1D2, which corresponds to a peak current of 6 A, pulse-on time of 70 µs, pulse-off time of 20 µs, and a tool rotation speed of 120 rpm. Likewise, from the Fig. 6(b) and 6(c) optimal parametric combination for DO and TWR is $A_1B_1C_3D_3$ and $A_1B_1C_1D_3$ respectively. Therefore, it confirms that, higher value of peak current and pulse-on-time leads to higher MRR, DO and TWR as discussed earlier.

Table 4 — L_{16} Design of experiments and Results

SR. No.	A	B	C	D	Avg. MRR (mg/min)	S/N ratio	Avg. DO (µm)	S/N ratio	Avg. TWR (mm/min)	S/N ratio
1	3	40	20	110	3.45	10.7564	63	−35.987	0.46	6.83977
2	3	50	30	120	3.9	11.8213	69	−36.777	0.56	5.03624
3	3	60	40	130	4.05	12.1491	67	−36.521	0.70	3.09804
4	3	70	50	140	5.1	14.1514	73	−37.266	0.98	0.17548
5	4	40	30	130	4.8	13.6248	66	−36.391	0.77	2.27019
6	4	50	20	140	5.7	15.1175	71	−37.025	0.88	1.15984
7	4	60	50	110	5.55	14.8859	68	−36.65	1.33	−2.477
8	4	70	40	120	7.65	17.6732	73	−37.266	1.72	−4.6853
9	5	40	40	140	6.15	15.7775	78	−37.842	1.96	−5.8451
10	5	50	50	130	6.3	15.9868	81	−38.17	2.00	−5.9989
11	5	60	20	120	8.7	18.7904	89	−38.988	2.38	−7.5315
12	5	70	30	110	9.6	19.6454	94	−39.463	2.42	−7.6583
13	6	40	50	120	7.95	18.0073	85	−38.588	2.24	−7.005
14	6	50	40	110	8.85	18.9389	87	−38.79	2.63	−8.3826
15	6	60	30	140	9.45	19.5086	91	−39.181	2.66	−8.4976
16	6	70	20	130	10.35	20.2988	97	−39.735	2.73	−8.7233

ANOVA for MRR, DO and TWR

For the identification of significant process parameters and their contribution during machining in determining the output responses, analysis of variance (ANOVA) can be effectively utilised. The ANOVA results for MRR, DO, and TWR are presented in Table 5. P-values are in ANOVA table used to identify the significant parameters for responses. Parameters

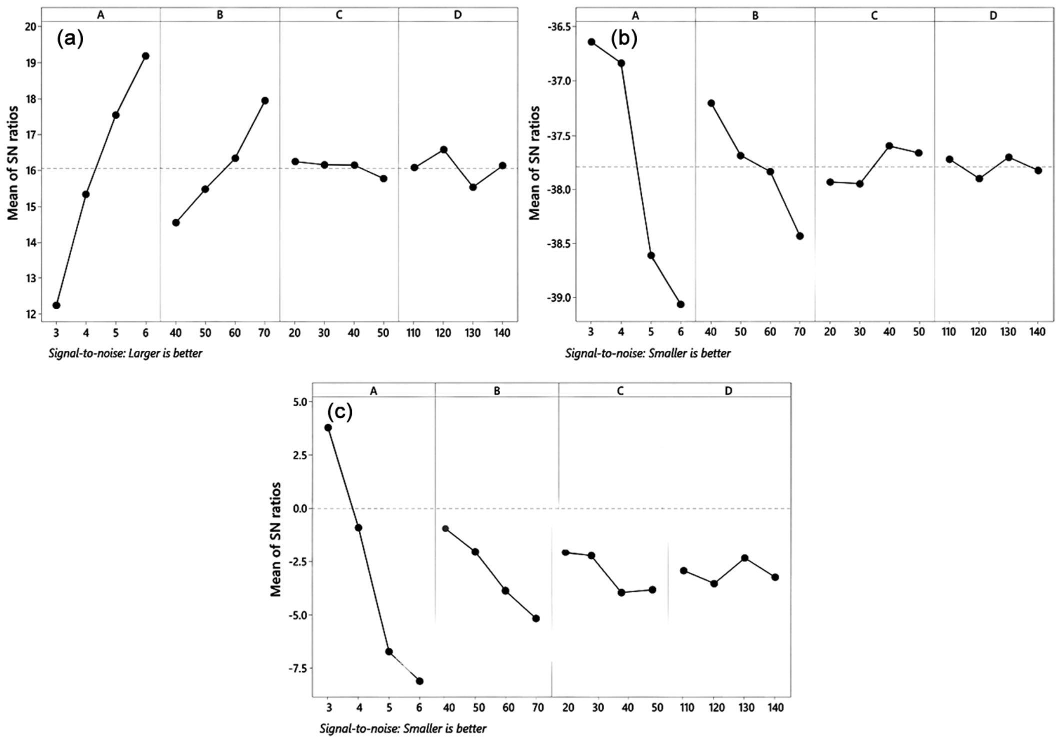

Fig. 6 — S/N ratio graphs for mean of: (a) MRR, (b) DO, (c) TWR

Table 5 — ANOVA for different output responses

For MRR (mg/min)

Source	DF	Adj SS	Adj MS	F-Value	P-Value	% Contri.
A	3	56.828	18.9427	166.3	0.001	76.01
B	3	14.9217	4.9739	43.67	0.006	19.96
C	3	1.613	0.5377	4.72	0.117	2.16
D	3	1.0505	0.3502	3.07	0.191	1.41
Error	3	0.3417	0.1139	—	—	0.46
Total	15	74.7548	—	—	—	—

For DO (μm)

Source	DF	Adj SS	Adj MS	F-Value	P-Value	% contri.
A	3	1489	496.333	129.48	0.001	82.04
B	3	261.5	87.167	22.74	0.014	14.41
C	3	49.5	16.5	4.3	0.131	2.73
D	3	3.5	1.167	0.3	0.823	0.19
Error	3	11.5	3.833	—	—	0.63
Total	15	1815	—	—	—	—

For TWR (mm/min)

Source	DF	Adj SS	Adj MS	F-Value	P-Value	% contri.
A	3	9.2197	3.07322	174.02	0.001	89.79
B	3	0.859	0.28634	16.21	0.023	8.37
C	3	0.0567	0.01889	1.07	0.479	0.55
D	3	0.0793	0.02644	1.5	0.374	0.77
Error	3	0.053	0.01766	—	—	0.52
Total	15	10.2676	—	—	—	—

Table 6 — Confirmation experiment results

Output response	Initial parametric setting ($A_2B_2C_2D_2$)	Optimal parametric setting	% improvement due to optimization
MRR (mg/min)	5.64	$A_4B_4C_1D_2$ 11.93	111.52
DO (μm)	72	$A_1B_1C_3D_3$ 57	20.83
TWR (mm/min)	1.12	$A_1B_1C_1D_3$ 0.26	76.79

where, A = Peak current, B = Pulse-on-time , C = Pulse-off-time , D = Tool rotation

Table 7 — Results based on GRA analysis

Sr. No.	Normalization			Deviation sequence			Grey relational coefficient			GRG	Rank
	MRR	DO	TWR	MRR	DO	TWR	MRR	DO	TWR		
1	0.0000	1.0000	1.0000	1.0000	0.0000	0.0000	0.3333	1.0000	1.0000	0.7778	1
2	0.0652	0.8235	0.9559	0.9348	0.1765	0.0441	0.3485	0.7391	0.9190	0.6689	3
3	0.0870	0.8824	0.8943	0.9130	0.1176	0.1057	0.3538	0.8095	0.8255	0.6629	4
4	0.2391	0.7059	0.7709	0.7609	0.2941	0.2291	0.3966	0.6296	0.6858	0.5707	7
5	0.1957	0.9118	0.8634	0.8043	0.0882	0.1366	0.3833	0.8500	0.7855	0.6729	2
6	0.3261	0.7647	0.8150	0.6739	0.2353	0.1850	0.4259	0.6800	0.7299	0.6119	5
7	0.3043	0.8529	0.6167	0.6957	0.1471	0.3833	0.4182	0.7727	0.5661	0.5857	6
8	0.6087	0.7059	0.4449	0.3913	0.2941	0.5551	0.5610	0.6296	0.4739	0.5548	9
9	0.3913	0.5588	0.3392	0.6087	0.4412	0.6608	0.4510	0.5313	0.4307	0.4710	15
10	0.4130	0.4706	0.3216	0.5870	0.5294	0.6784	0.4600	0.4857	0.4243	0.4567	16
11	0.7609	0.2353	0.1542	0.2391	0.7647	0.8458	0.6765	0.3953	0.3715	0.4811	13
12	0.8913	0.0882	0.1366	0.1087	0.9118	0.8634	0.8214	0.3542	0.3667	0.5141	10
13	0.6522	0.3529	0.2159	0.3478	0.6471	0.7841	0.5897	0.4359	0.3894	0.4717	14
14	0.7826	0.2941	0.0441	0.2174	0.7059	0.9559	0.6970	0.4146	0.3434	0.4850	12
15	0.8696	0.1765	0.0308	0.1304	0.8235	0.9692	0.7931	0.3778	0.3403	0.5037	11
16	1.0000	0.0000	0.0000	0.0000	1.0000	1.0000	1.0000	0.3333	0.3333	0.5556	8

having P-Value < 0.05 can be considered as the significant parameters for machining. From the Tables 5–7, peak current and pulse-on-time (P-Value < 0.05) was found significant for MRR, DO and TWR. No other parameters or their combination were found significant for μ-EDD of processed Zn/(Fe+Ag+Mg)-MMC.

Confirmation Test

Confirmation test were performed to forecast and estimate the performance of optimised process parametric combination. The confirmation test results obtained at the optimal process parameters along with the percentage improvement in the responses compared with the initial parameter settings, i.e. the second level of all process parameters, are presented in Table 6. From the test results it has been found that MRR, DO and TWR improved by 111.52%, 20.83%, 76.79% respectively when compared to the initial experimental parameter setting.

Development of Regression Model

Based on the experimental results; correlation between output response and process parameters have been developed using Minitab 19 software. Equations 4–6 represent the mathematical relations between responses (MRR, DO and TW) and process variables (peak current, pulse-on-time, pulse-off-time and tool rotation).

$$MRR = -2.75 + 1.6837\,A + 0.08513\,B - 0.02737\,C - 0.01463\,D \quad \ldots (4)$$

$$R^2_{MRR} = 97.81$$

$$DO = 27.2 + 8.200\,A + 0.3550\,B - 0.1350\,C - 0.0050\,D \quad \ldots (5)$$

$$R^2_{OC} = 99.37$$

$$TWR = -2.027 + 0.6685\,A + 0.02065\,B + 0.00228\,C - 0.00438\,D \quad \ldots (6)$$

$$R^2_{TW} = 99.48$$

Here, R² denotes the coefficient of multiple determination and represents the fraction of total response variation explained by the selected regression variables. The regression coefficients A, B, C, and D were obtained using the mathematical relationships given in Eqs 4–6. Normal probability plots for MRR, DO, and TWR are presented in Fig. 7(a–c), respectively. The linear distribution of residuals along the reference line indicates normal error distribution. To validate the

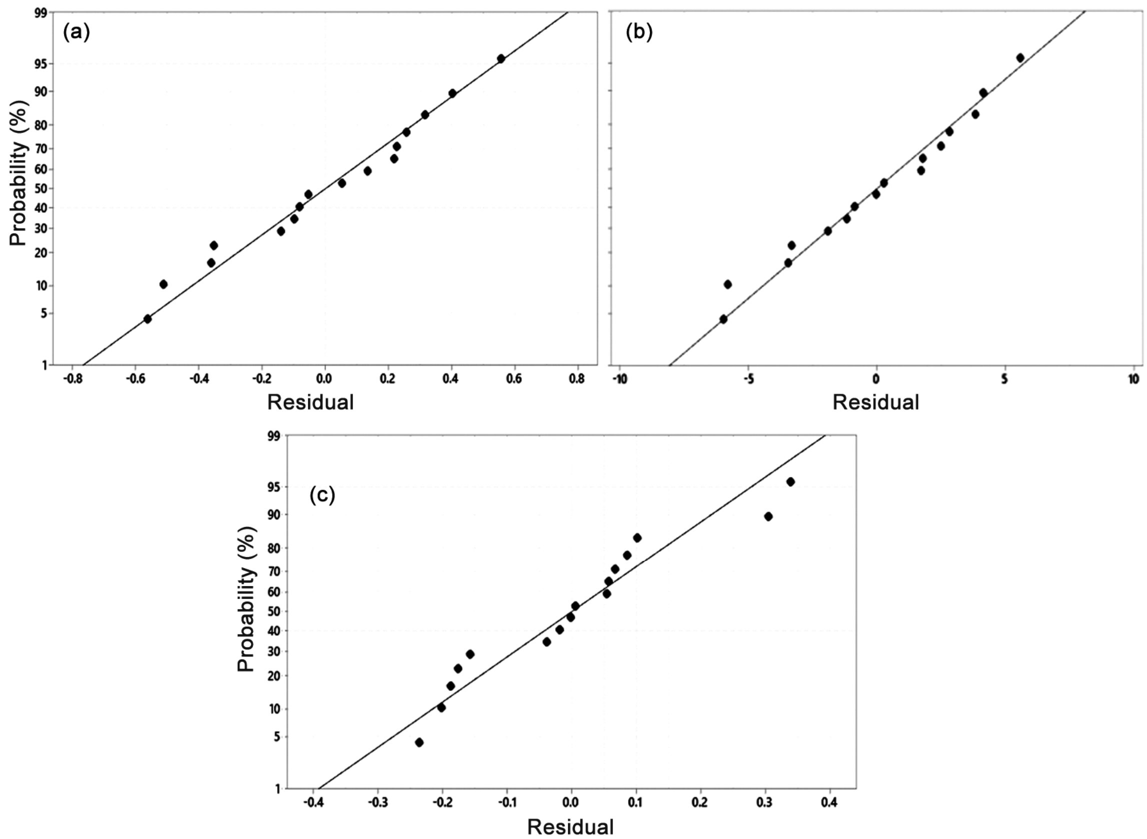

Fig. 7 — Normal probability plots for: (a) MRR, (b) DO, (c) TWR

regression models, sixteen experimental conditions were analysed. The results demonstrate that the developed regression models are accurate and reliable for estimating the responses during micro-drilling.

Grey Relational Analysis (GRA) based Optimization

GRA is a multi-response optimization method that identifies the combination of process parameters at which all the responses show comparatively better performance. GRA normalize the output responses in the range of 0 and 1. For the normalization of responses Eqs 7 and 8 were utilised.

Normalized value for responses having larger the better criteria i.e. MRR can be given as:

$$x_i^n(k)\frac{x_i(k) - min\, x_i(k)}{max\, x_i(k) - min\, x_i(k)} \qquad \dots (7)$$

Normalized value for the responses having lower the better criteria i.e DO and TWR can be given as:

$$x_i^m(k)\frac{max\, x_i(k) - x_i(k)}{max\, x_i(k) - min\, x_i(k)} \qquad \dots (8)$$

Here, i = 1, 2, …, m represents the number of experimental trials, while k = 1, 2, …, n denotes the number of response variables. The term $x_i(k)$ refers to the original experimental data, and $x_i^n(k)$ and $x_i^m(k)$ indicate the normalized response values. The terms max $x_i(k)$ and min $x_i(k)$ correspond to the maximum and minimum values obtained from the nth and mth experiments, respectively.[39]

Normalised values used to calculate the deviation sequence utilising Eq. 9 given as follows:

$$\Delta_{oi} = \| x_o(k) - x_i(k) \| \qquad \dots (9)$$

where, $x_0(k)$ represents the maximum value in the normalized data column, which is equal to 1.

Further, the Grey relation coefficient (GRC) is evaluated by using the deviation values and is calculated using Eq. 10.

$$\xi_i(k) = \frac{\Delta_{min} + (\xi^k \Delta_{max})}{\Delta_{oi}(k) + (\xi^k \Delta_{max})} \qquad \dots (10)$$

where, ξ is identification or distinguishing coefficient having range from 0 to 1; usually taken as 0.5 while calculating GRC.[40]

Additionally, Grey Relational Grade (GRG) can be calculated as the weighted sum of GRC values. Rank 1 is given to the maximum GRG value and last rank is given to the minimum GRG value. It indicates the best parametric combination to secure the optimum product quality having the maximum GRG ranking.

The normalized values, deviation sequences, GRC values, GRG values, and their corresponding ranks are presented in Table 7.

The response table for GRG is presented in Table 8, whereas the S/N ratio plots associated with the grey relational grades are shown in Fig. 8. Larger GRG values represent improved multiple response quality. Therefore, based on Table 8 and Fig. 8, it can be said that the parametric combination for the multi-response optimization is $A_1B_1C_1D_1$, which is nothing but first parametric combination of Taguchi's L_{16} based orthogonal array (Table 4).

ANOVA for GRG

The ANOVA results for GRG values are presented in Table 9. From the Table 9, peak current and pulse-off-time has been found as the significant parameters (as P-value < 0.05) for response characteristics contributing 72.96% and 14.66% respectively. Rotation of tool electrode also cannot be neglected as it has P-Value very close to 0.05 i.e. 0.053.

Confirmation test for GRA based Optimization

For the confirmation of GRA based optimization, the tests were again performed at $A_1B_1C_1D_1$ parametric combination with 3 replications and average result was used for comparison and represented in Table 10. From the Table 10 it can be seen that at parametric combination based on GRA, MRR is worsen by 37.76% whereas, DO and TWR improved by 13.89% and 57.14% respectively.

Analysis of Micro-drilled hole via SEM

The surface texture obtained from any machining process play an eminent role in deciding its application in various field. The analysis of micro-drilled hole can be effectively performed by scanning electrode microscopy (SEM) examination. SEM micrographs of the micro-drilled holes on the developed Zn/(Fe+Ag+Mg)-MMC specimen are shown in Fig. 9(a–j). The measurement of hole dimensions was carried out using Image J software. The drilled holes with three replications under the initial parameter setting, i.e. $A_2B_2C_2D_2$ are shown in Fig. 9 (a). SEM images of the micro-drilled holes obtained under the optimal parameter settings for MRR, DO, and TWR are presented in Fig. 9(b–c), 9(d–e), and 9(f–g), respectively. From the Fig. 9 (b–c) high ovality, burrs/fins and damage were identified at the periphery of machined hole whereas Fig. 9 (d–e) represent high circularity and less surface damage & presence of fins. Fig. 9 (h-i) illustrates the SEM image of the drilled hole under optimal parameter setting based on GRA i.e. $A_1B_1C_1D_1$. Figure approves high circularity and lower DO. This occurs due to the

Table 8 — GRG response table

Level	A	B	C	D
1	0.6701	0.5983	0.6066	0.5906
2	0.6063	0.5556	0.5899	0.5441
3	0.4807	0.5584	0.5434	0.587
4	0.504	0.5488	0.5212	0.5393
Difference	0.1893	0.0496	0.0854	0.0513
Rank	1	4	2	3

Table 9 — ANOVA for GRG

Source	DF	Adj SS	Adj MS	F-Value	P-Value	% Contri.
A	3	0.09429	0.03143	92.92	0.002	72.96
B	3	0.00602	0.00201	5.94	0.089	4.66
C	3	0.01895	0.00632	18.67	0.019	14.66
D	3	0.00895	0.00298	8.82	0.053	6.93
Error	3	0.00102	0.00034	—	—	0.79
Total	15	0.12923	—	—	—	—

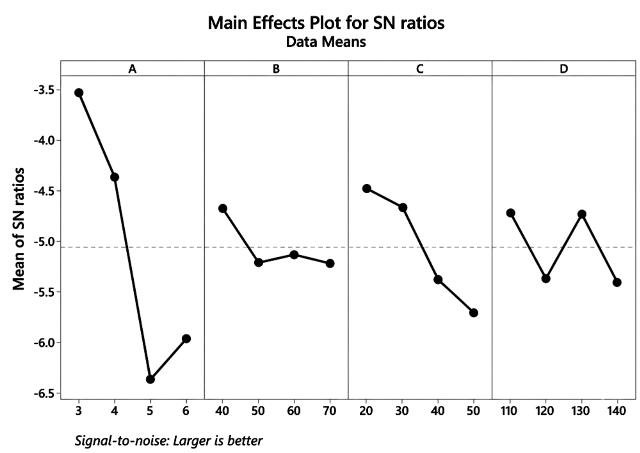

Fig. 8 — S/N ratio graph for GRG

Table 10 — Confirmation test results based on GRA optimization

Responses	Initial parameters ($A_2B_2C_2D_2$)	Optimal parameters ($A_1B_1C_1D_1$)	% improvement due to optimization
MRR (mg/min)	5.64	3.51	−37.76
DO (μm)	72	62	13.89
TWR (mm/min)	1.12	0.48	57.14

where, A = Peak current, B = Pulse-on-time , C = Pulse-off-time, D = Tool rotation

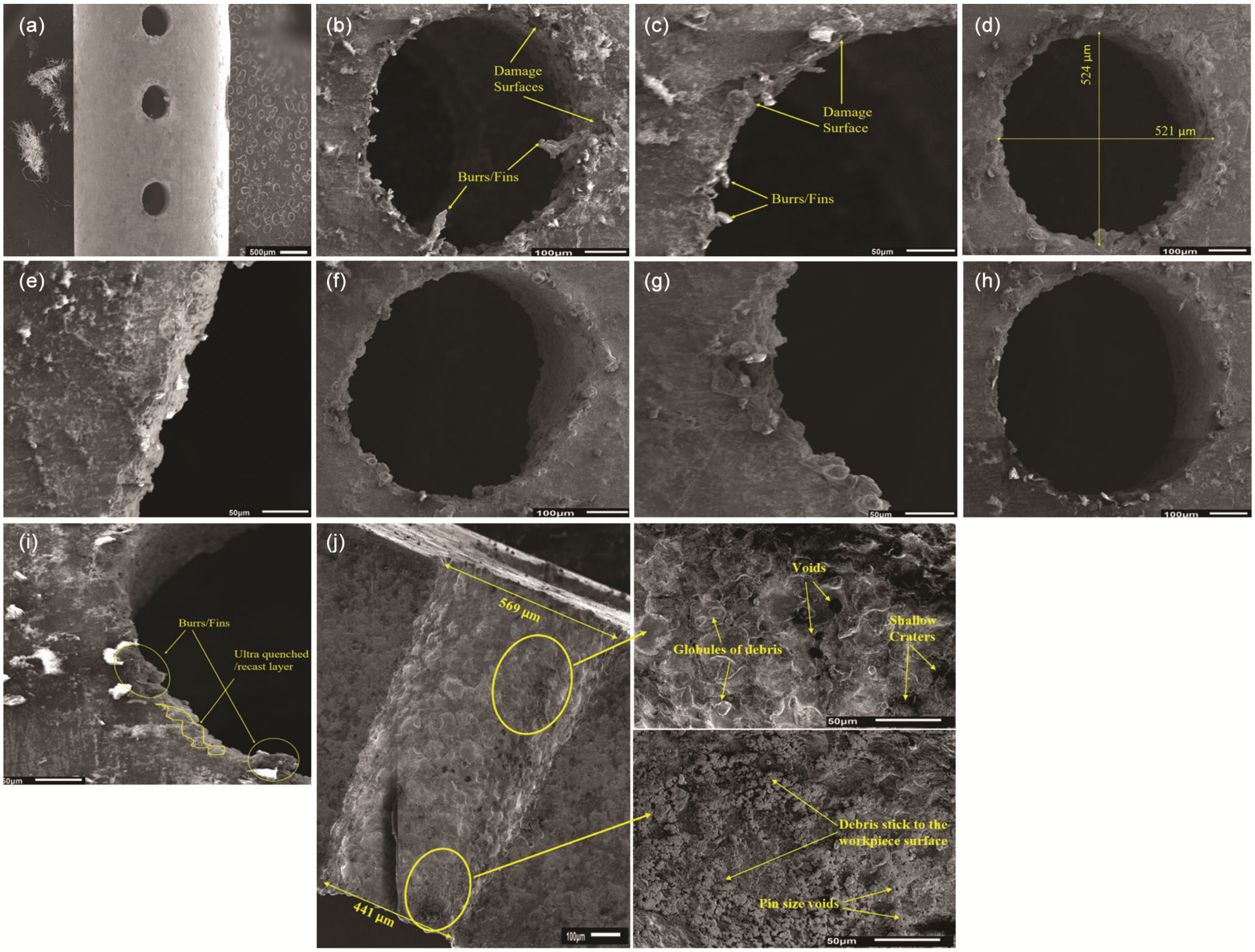

Fig. 9 — SEM micrographs of micro-drilled hole at: (a) initial parameter setting i.e. $A_2B_2C_2D_2$, (b) optimal parameter set for MRR i.e. $A_4B_4C_1D_2$, (c) surface profile at optimal set of parameters for MRR, (d) optimal set of parameters for DO i.e. $A_1B_1C_3D_3$, (e) surface profile at optimal set of parameters for DO, (f) optimal set of parameters for TWR i.e. $A_1B_1C_1D_3$, (g) surface profile at optimal set of parameters, (h) optimal set of parameters based on GRA i.e. $A_1B_1C_1D_1$, (i) surface profile at optimal set of parameters based on GRA, (j) cross sectional image of drilled hole at optimal set of parameters for MRR

lower values of tool rotation, peak current and pulse-on time which result in weaker spark generation for a shorter duration along with reduced tool vibration. Only a limited number of ultra-quenched spots were found on the periphery of machined surface. Under this parameter setting only a small number of minor burrs and fins were formed on the periphery of surface when compared with Fig. 9(b–c).

The cross-sectional image of the micro-drilled hole at the optimal set of parameters for MRR is shown in Fig. 9(j). The presence of features such as globules of debris, voids, and shallow craters on the machined surface is confirmed in Fig. 9(j). It may be due to the generation of thermal stresses during machining due because of strong sparks as the peak current and pulse-on-time both are high at the optimal setting for MRR. Thermal stresses also generated due to non-uniform distribution of temperature along the machined surface.[36] It can be noted that these features remain shallow and uniformly distributed which is typical under low-energy µ-EDD. Therefore, they do not significantly affect the dimensional accuracy, roundness, or load-bearing capability of the micro-drilled holes. Such surface textures mainly influence surface integrity, not bulk structural strength, because they are confined to a very thin recast layer.[41,42] However, if these features had been deeper, sharper, or associated with micro cracks, they could have acted as local stress concentrators and potentially affecting fatigue and corrosion performance. Maintaining optimized discharge energy and proper dielectric flushing helps ensure that these micro-features remain small and rounded, thereby minimizing any adverse impact on the mechanical reliability of the micro-drilled holes.

The adhesion of debris on the workpiece surface at higher depth is also observed in Fig. 9(j). At higher depths both overcut and tool wear have a major influence on machining accuracy.[43] The inside surface of micro-drilled hole affected by the interrupting sparking which may be caused by higher value of peak current and pulse-on-time. Apart from that, figure also shows the tapering in the drilled hole which is highly affected by the rotation and vibration created by the tool electrode.

Conclusions

In the current experimental study, Zn/(Fe+Ag+Mg)-MMC was successfully fabricated via ultrasonic vibration-assisted stir casting and investigated its micro-electrical discharge drilling (μ-EDD) characteristics for potential biodegradable cardiovascular stent applications. The developed composite exhibited enhanced tensile strength, microhardness, and ductility compared with pure zinc, addressing one of the major limitations of Zn-based biodegradable stent materials. The experimental results further demonstrated that machining performance was significantly influenced by peak current, pulse-on time, pulse-off time, tool rotation, tool material, and polarity conditions. Among the investigated tool–polarity combinations, the copper tool electrode operated under positive polarity exhibited superior machining performance. Taguchi-based optimization resulted in improvements of 111.52%, 20.83%, and 76.79% in material removal rate (MRR), drill overcut (DO), and Tool Wear Rate (TWR), respectively, at their corresponding optimal parameter settings, while Grey Relational Analysis (GRA) effectively identified the optimum conditions for simultaneous multi-response optimization. SEM analysis of the machined micro-holes confirmed acceptable surface integrity and high hole quality under optimized conditions. Future investigations into corrosion behaviour, antibacterial performance, biocompatibility and degradation characteristics through in vitro and in vivo studies will be essential to fully validate the material's suitability for cardiovascular stent applications and confirm its long-term physiological performance

Acknowledgement

The authors sincerely acknowledge the Department of Metallurgy and Materials Engineering PEC Chandigarh for granting access to the testing facilities.

Declaration

The authors declare that there is no conflict of interest regarding the authorship, investigation, or publication of this article.

References

1 Hanawa T, Materials for metallic stents, *J Artif Organs*, **12(2)** (2009) 73–79, doi: 10.1007/s10047-008-0456-x.

2 Toong D W Y, Ng J C K, Huang Y, Wong P E H, Leo H L, Venkatraman S S & Ang H Y, Bioresorbable metals in cardiovascular stents: Material insights and progress, Materialia, **12** (2020) 100727, doi: 10.1016/j.mtla.2020.100727.

3 Eberhart R C, Su S H, Nguyen K T, Zilberman M, Tang L, Nelson K D & Frenkel P, Bioresorbable polymeric stents: current status and future promise, J Biomater Sci Polym Ed, **14(4)** (2003) 299–312, doi: 10.1163/156856203321478838.

4 Im S H, Jung Y & Kim S H, Current status and future direction of biodegradable metallic and polymeric vascular scaffolds for next-generation stents, Acta Biomater, **60** (2017) 3–22, doi: 10.1016/j.actbio.2017.07.019.

5 Ang H Y, Huang Y Y, Lim S T, Wong P, Joner M & Foin N, Mechanical behavior of polymer-based vs. metallic-based bioresorbable stents, *J Thorac Dis*, **9(Suppl 9)** (2017) S923–S934, doi: 10.21037/jtd.2017.06.30.

6 Witte F, The history of biodegradable magnesium implants: a review, *Acta Biomater*, **6(5)** (2010) 1680–1692, doi: 10.1016/j.actbio.2010.02.028.

7 Moravej M, Prima F, Fiset M & Mantovani D, Electroformed iron as new biomaterial for degradable stents: Development process and structure–properties relationship, *Acta Biomater*, **6(5)** (2010) 1726–1735, doi: 10.1016/j.actbio.2010.01.010.

8 Sotoudehbagha P, Sheibani S, Khakbiz M, Ebrahimi-Barough S & Hermawan H, Novel antibacterial biodegradable Fe–Mn–Ag alloys produced by mechanical alloying, *Mater Sci Eng C*, **88** (2018) 88–94, doi: 10.1016/j.msec.2018.03.005.

9 Stoeckel D, Pelton A & Duerig T, Self-expanding nitinol stents: material and design considerations, *Eur Radiol*, **14(2)** (2004) 292–301, doi: 10.1007/s00330-003-2022-5.

10 Hu W & Jiang J, Hypersensitivity and in-stent restenosis in coronary stent materials, *Front Bioeng Biotechnol*, **10** (2022) 1003322, doi: 10.3389/fbioe.2022.1003322.

11 Bowen P K, Drelich J & Goldman J, Zinc exhibits ideal physiological corrosion behavior for bioabsorbable stents, *Adv Mater*, **25(18)** (2013) 2577–2582, doi: 10.1002/adma.201300226.

12 Bowen P K, Shearier E R, Zhao S, Guillory R J, Zhao F, Goldman J & Drelich J W, Biodegradable metals for cardiovascular stents: from clinical concerns to recent Zn-alloys, *Adv Healthc Mater*, **5(10)** (2016) 1121–1140, doi: 10.1002/adhm.201501019.

13 Hiebl B, Nennig E, Schiestel S, Kovacs A, Jung F & Fischer H, Biocompatibility of a novel zinc stent with a closed-cell-design, *Clin Hemorheol Microcirc*, **61(2)** (2015) 205–211, doi: 10.3233/CH-151983.

14 Yang H, Wang C, Liu C, Chen H, Wu Y, Han J, Jia Z, Yang G, Wu S, Yuan W & Zheng Y, Evolution of the degradation mechanism of pure zinc stent in the one-year study of rabbit abdominal aorta model, *Biomaterials*, **145** (2017) 92–105, doi: 10.1016/j.biomaterials.2017.08.022.

15 Liu L, Meng Y, Dong C, Yan Y, Volinsky A A & Wang L N, Initial formation of corrosion products on pure zinc in simulated

body fluid, *J Mater Sci Technol*, **34(12)** (2018) 2271–2282, doi: 10.1016/j.jmst.2018.05.005.

16 Li P, Schille C, Schweizer E, Rupp F, Heiss A, Legner C, Koller M, Hort N & Scheideler L, Mechanical characteristics, in vitro degradation, cytotoxicity, and antibacterial evaluation of Zn-4.0 Ag alloy as a biodegradable material, *Int J Mol Sci*, **19(3)** (2018) 755, doi: 10.3390/ijms19030755.

17 Kafri A, Ovadia S, Goldman J, Drelich J & Aghion E, The suitability of Zn–1.3% Fe alloy as a biodegradable implant material, *Metals*, **8(3)** (2018) 153, doi: 10.3390/met8030153.

18 Niu J, Tang Z, Huang H, Pei J, Zhang H, Yuan G & Ding W, Research on a Zn–Cu alloy as a biodegradable material for potential vascular stents application, *Mater Sci Eng C*, **69** (2016) 407–413, doi: 10.1016/j.msec.2016.06.082.

19 Mostaed E, Sikora-Jasinska M, Mostaed A, Loffredo S, Demir A G, Previtali B, Mantovani D & Vedani M, Novel Zn-based alloys for biodegradable stent applications: Design, development and in vitro degradation, *J Mech Behav Biomed Mater*, **60** (2016) 581–602, doi: 10.1016/j.jmbbm.2016.03.018.

20 Vojtěch D, Kubásek J, Šerák J & Novák P, Mechanical and corrosion properties of newly developed biodegradable Zn-based alloys for bone fixation, *Acta Biomater*, **7(9)** (2011) 3515–3522, doi: 10.1016/j.actbio.2011.05.008.

21 Sikora-Jasinska M, Mostaed E, Mostaed A, Beanland R, Mantovani D & Vedani M, Fabrication, mechanical properties and in vitro degradation behavior of newly developed Zn–Ag alloys for degradable implant applications, *Mater Sci Eng C*, **77** (2017) 1170–1181, doi: 10.1016/j.msec.2017.04.023.

22 Zhao L, Xie Y, Zhang Z, Wang X, Qi Y, Wang T, Li S & Cui C, Fabrication and properties of biodegradable ZnO nano-rods/porous Zn scaffolds, *Mater Charact*, **144** (2018) 227–238, doi: 10.1016/j.matchar.2018.07.023.

23 Hehrlein C, Schorch B, Kress N, Arab A, von Zur Mühlen C, Bode C, Wendel H P & Nennig E, Zn-alloy provides a novel platform for mechanically stable bioresorbable vascular stents, *PLoS One*, **14(1)** (2019) e0209111, doi: 10.1371/journal.pone.0209111.

24 Fu J, Su Y, Qin Y X, Zheng Y, Wang Y & Zhu D, Evolution of metallic cardiovascular stent materials: a comparative study among stainless steel, magnesium and zinc, *Biomaterials*, **230** (2020) 119641, doi: 10.1016/j.biomaterials.2019.119641.

25 Waksman R, Late thrombosis after radiation: sitting on a time bomb, *Circulation*, **100(8)** (1999) 780–782, doi: 10.1161/01.CIR.100.8.780.

26 Joner M, Finn A V, Farb A, Mont E K, Kolodgie F D, Ladich E, Kutys R, Skorija K, Gold H K & Virmani R, Pathology of drug-eluting stents in humans: delayed healing and late thrombotic risk, *J Am Coll Cardiol*, **48(1)** (2006) 193–202, doi: 10.1016/j.jacc.2006.03.042.

27 Saxena K K, Qian J & Reynaerts D, Development and investigations on a hybrid tooling concept for coaxial and concurrent application of electrochemical and laser micromachining processes, *Precis Eng*, **65** (2020) 171–184, doi: 10.1016/j.precisioneng.2020.05.014.

28 Malik A & Manna A, Study on precision microholes using pulsed laser with jet electrochemical machining, *Arab J Sci Eng*, **43(9)** (2018) 4593–4608, doi: 10.1007/s13369-017-2998-9.

29 Kumar L & Kumar K, Investigating the electrical discharge micro drilling for porous architecture in magnesium alloy, *Int J Lightweight Mater Manuf*, **5(3)** (2022) 339–351, doi: 10.1016/j.ijlmm.2022.04.001.

30 Prakash V, Kumar P, Singh P K, Hussain M, Das A K & Chattopadhyaya S, Micro-electrical discharge machining of difficult-to-machine materials: a review, *Proc Inst Mech Eng B J Eng Manuf*, **233(2)** (2019) 339–370, doi: 10.1177/0954405417718591.

31 Kibria G, Jahan M P & Bhattacharyya B, Micro-electrical discharge machining processes: Technologies and applications, (Springer, Singapore) 2019, doi: 10.1007/978-981-13-3074-2.

32 Xing Q, Yao Z & Zhang Q, Effects of processing parameters on processing performances of ultrasonic vibration-assisted micro-EDM, *Int J Adv Manuf Technol*, **112(1)** (2021) 71–86, doi: 10.1007/s00170-020-06357-9.

33 Mohan P & Manna A, Fabrication and processing of bioabsorbable hybrid Zn/(Ag+Fe+Mg)-MMC on developed ultrasonic vibration-assisted argon atmosphere stir casting set-up, *Arab J Sci Eng*, **47(7)** (2022) 8361–8372, doi: 10.1007/s13369-021-06205-2.

34 Chechi P, Maurya S K, Prasad R & Manna A, Influence on microstructural and mechanical properties of Al2O3/graphite/flyash-reinforced hybrid composite using scrap aluminum alloy, *Int J Metalcast*, **18(2)** (2024) 975–986, doi: 10.1007/s40962-023-01069-8.

35 Maurya S K, Susheel C K & Manna A, Experimental investigation of wire EDM parameters during machining of fabricated hybrid Al/(SiC+ZrO2+NiTi)-MMC, *Adv Mater Process Technol*, **10(2)** (2024) 187–197, doi: 10.1080/2374068X.2022.2109684.

36 Maurya S K, Ghosal A & Manna A, Experimental investigations during fabrication and electrical discharge machining of hybrid Al/(SiC+ZrO2+NiTi) MMC, *Int J Mach Machinability Mater*, **24(3–4)** (2022) 215–230, doi: 10.1504/IJMMM.2022.125195.

37 Kuppan P, Narayanan S, Oyyaravelu R & Balan A S S, Performance evaluation of electrode materials in electric discharge deep hole drilling of Inconel 718 superalloy, *Procedia Eng*, **174** (2017) 53–59, doi: 10.1016/j.proeng.2017.01.141.

38 Abifarin J K, Taguchi grey relational analysis on the mechanical properties of natural hydroxyapatite: effect of sintering parameters, *Int J Adv Manuf Technol*, **117(1)** (2021) 49–57, doi: 10.1007/s00170-021-07288-9.

39 Dixit N & Jain P K, Multi-objective strength optimization of fused filament fabricated complex flexible parts using grey relational analysis, *Iran J Sci Technol Trans Mech Eng*, **47(4)** (2023) 1787–1797, doi: 10.1007/s40997-022-00589-8.

40 Kumar P & Hussain M, Effects of Micro-EDM parameters on the surface integrity of the micro-holes fabricated on nickel sheet, in Recent trends in mechanical engineering: Select proceedings of ICIME 2019, (Springer, Singapore) 2020, 259–270, doi: 10.1007/978-981-15-1124-0_23.

41 Wang C, Wang H, Chu X, Lu Y & He H, Study on forming mechanism of the recast layer on the workpiece surface during micro EDM, *Materials*, **17(5)** (2024) 1073, doi: 10.3390/ma17051073.

42 Arab J & Dixit P, Influence of tool electrode feed rate in the electrochemical discharge drilling of a glass substrate, *Mater Manuf Process*, **35(15)** (2020) 1749–1760, doi: 10.1080/10426914.2020.1784936.

43 Zhang M, Liu E, Xiao X, Yu S, Li H, Wang K, Chen Y & Li Z, Microstructure, mechanical properties and in vitro degradation properties of ZnFe alloys, *Mater Charact*, **192** (2022) 112220, doi: 10.1016/j.matchar.2022.112220.